Biophysical Journal
Article

Biophysical Society

Phonons reveal coupled cholesterol-lipid dynamics in ternary membranes

James E. Fitzgerald III,[1] Dmytro Soloviov,[2,3] Yong Q. Cai,[4] Frederick A. Heberle,[5] Daisuke Ishikawa,[6,7] Alfred Q. R. Baron,[6,7] Dima Bolmatov,[8,9,*] Mikhail Zhernenkov,[4,*] and Edward R. Lyman[1,10,*]

[1]Department of Physics & Astronomy, University of Delaware, Newark, Delaware; [2]European Molecular Biology Laboratory, Hamburg Outstation c/o DESY, Hamburg, Germany; [3]Institute for Safety Problems of Nuclear Power Plants of the Ukrainian NAS, Kyiv, Ukraine; [4]National Synchrotron Light Source II, Brookhaven National Laboratory, Upton, New York; [5]Department of Chemistry, University of Tennessee, Knoxville, Tennessee; [6]Materials Dynamics Laboratory, RIKEN SPring-8 Center, Sayo, Hyogo, Japan; [7]Precision Spectroscopy Division, CSRR, SPring-8/JASRI, Sayo, Hyogo, Japan; [8]Department of Physics and Astronomy, University of Tennessee, Knoxville, Tennessee; [9]Shull-Wollan Center, Oak Ridge National Laboratory, Oak Ridge, Tennessee; and [10]Department of Chemistry & Biochemistry, University of Delaware, Newark, Delaware

ABSTRACT Experimental studies of collective dynamics in lipid bilayers have been challenging due to the energy resolution required to observe these low-energy phonon-like modes. However, inelastic x-ray scattering (IXS) measurements—a technique for probing vibrations in soft and biological materials—are now possible with sub-meV resolution, permitting direct observation of low-energy, phonon-like modes in lipid membranes. Here, IXS measurements with sub-meV energy resolution reveal a low-energy optic-like phonon mode at roughly 3 meV in the liquid-ordered (L_o) and liquid-disordered phases of a ternary lipid mixture. This mode is only observed experimentally at momentum transfers greater than 5 nm^{-1} in the L_o system. A similar gapped mode is also observed in all-atom molecular dynamics (MD) simulations of the same mixture, indicating that the simulations accurately represent the fast, collective dynamics in the L_o phase. Its optical nature and the Q range of the gap together suggest that the observed mode is due to the coupled motion of cholesterol-lipid pairs, separated by several hydrocarbon chains within the membrane plane. Analysis of the simulations provides molecular insight into the origin of the mode in transient, nanoscale substructures of hexagonally packed hydrocarbon chains. This nanoscale hexagonal packing was previously reported based on MD simulations and, later, by NMR measurements. Here, however, the integration of IXS and MD simulations identifies a new signature of the L_o substructure in the collective lipid dynamics, thanks to the recent confluence of IXS sensitivity and MD simulation capabilities.

SIGNIFICANCE Fast-timescale, collective motions in membranes have been difficult to measure but are critical to understanding how the molecular scale crosses over to the mesoscale that determines functional dynamics (e.g., lipid and protein diffusion). This crossover is expected to be nontrivial in the case of cholesterol- and sphingolipid-rich liquid-ordered-like phases, which are characterized by the local ordering of hydrocarbon chains and subdiffusive dynamics. Here, integrated simulations and inelastic x-ray scattering measurements are shown to be a powerful new approach to obtaining the collective dynamics of phonon modes. Comparison between liquid-ordered and liquid-disordered phases reveals a unique dynamical signature of the liquid-ordered phase.

INTRODUCTION

Membrane fluidity emerged in the 1970s as a facet of cell membranes both fundamental and functional. Singer and Nicholson put forth their "fluid-mosaic" model (1), Sinensky showed that bacteria regulate membrane fluidity through lipid synthesis (2), and Saffman and Delbruck showed lateral diffusion to be phenomenologically rich, not exactly two-dimensional (2D) or 3D (3). In some cases, a clear functional rationale has been demonstrated for homeoviscous adaptation—bacterial membrane fluidity directly controls the diffusion of small-molecule electron carriers between complexes in the respiratory chain of *E. coli* and, therefore, the rate of respiration (4). Ernst and colleagues have identified mechanisms responsible for sensing fluidity in yeast, supporting the idea that fluidity is actively regulated (5).

Submitted March 16, 2024, and accepted for publication October 29, 2024.

*Correspondence: dbolmato@utk.edu or zhernenkov@gmail.com or elyman@udel.edu

Editor: Sarah Veatch.

https://doi.org/10.1016/j.bpj.2024.10.017

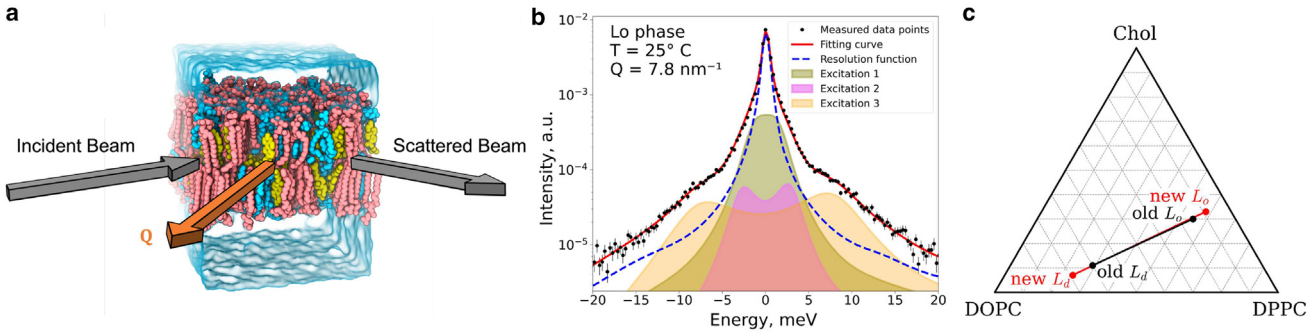

FIGURE 1 (*a*) In-plane scattering geometry of inelastic x-ray scattering (IXS) on the oriented lipid membrane. Both incident and scattered beams remain parallel to the membrane surface probing in-plane phonon excitations. (*b*) Example of an IXS spectrum of the ternary lipid mixture at momentum transfer 7.8 nm^{-1} in the L_o phase at 25°C. (*c*) New L_o-L_d tie-line endpoints determined via SAXS. For exact compositions and further details, see the supporting material.

However, the dynamic response of membranes is complex and scale dependent. Experimental measurements of viscosity report numbers varying by nearly two orders of magnitude. Fast-timescale, local measurements (e.g., based on chromophore dynamics) obtain values of 8–500 $\times$ 10^{-3} Pa s (6,7) across a range of temperatures and membrane lipid compositions. Longer-wavelength measurements that observe collective dynamics obtain values in the range 1.5–500 Pa s (8–13). Simulations necessarily access the faster, more local end of the spectrum and obtain values of 10–700 $\times$ 10^{-3} Pa s (14,15).

Dynamic scattering methods are uniquely positioned to resolve the scale-dependent dynamics of membranes, especially techniques that measure time- or frequency-dependent responses with momentum resolution. For example, neutron spin echo has been instrumental in measuring bending and thickness fluctuations (16–20). However, since neutron spin echo measures the self-part of the intermediate scattering function, it cannot directly inform on how individual molecular motions develop into the collective dynamics that determine transport properties such as viscosity and diffusion.

Inelastic x-ray scattering (IXS) has recently emerged as a unique and "molecular probe-free" tool for investigating the collective dynamics of biological membranes and interfaces at fundamental timescales (picoseconds) and length scales (nanometers) (21,22). Over the past decades, the intensity and resolution of IXS measurements at state-of-the-art facilities (SPring-8, APS, ESRF, NSLS II) have improved (23), which enables the observation of phonon excitations in soft (noncrystalline) materials including simple liquids (24–27), block copolymers (28), liquid crystals (mesogens) (29), and lipid membranes (30). When scattering from oriented stacks of bilayers, the in-plane collective dynamics of lipids (Fig. 1 *a*) are measured on timescales from 0.2 to 4 ps and momentum transfers from 1 to 25 nm^{-1} (corresponding length scales of 0.25–6 nm). Phonon spectra are obtained from the experimental data; typically, acoustic branches (propagating longitudinal and transverse modes) and optical modes (nonpropagating/breathing modes, standing waves) can be resolved. The length scales and timescales of IXS measurements are readily accessible to molecular dynamics (MD) simulation. Importantly, previous studies have demonstrated that the combination of IXS with MD simulations is especially powerful (31), offering a unique molecular picture of how local lipid motions crossover into collective dynamics and associated relaxation processes (32,33). This combination of approaches reveals their local and transient behavior, which is inaccessible to other techniques (34).

Here, we study the phonon excitations of a ternary lipid mixture of dipalmitoyl phosphocholine/dioleoyl phosphocholine/cholesterol (DPPC/DOPC/Chol) using small-angle x-ray scattering (SAXS), IXS, and all-atom MD simulations, focusing on the liquid-ordered (L_o) and liquid-disordered (L_d) phases. We first present SAXS measurements that suggest revised tie-line endpoints. The sensitivity of SAXS to small amounts of the minority phase indicates that previously published endpoints (35) were actually inside the two-phase region. These new data informed the preparation of pure L_o and L_d mixtures for IXS measurements and MD simulations. The IXS measurements reveal a low-energy "gapped" optical phonon mode, which only appears at wavenumbers above $Q = 4.5$ nm^{-1}. Calculation of phonon dispersions from the simulation data obtained spectra similar to those obtained experimentally, including the gapped mode. Analysis of the molecular packing in the simulation suggests that the gapped mode originates in locally ordered hydrocarbon chains, which are hexagonally ordered on scales of only a few lipids (36,37). Together, the two approaches reveal how the collective dynamics of ternary lipid mixtures change as the Chol concentration increases, suggesting significant contributions from coupled Chol/saturated lipid pairs in physiological membranes. More broadly, the results help establish integrated IXS/simulation analysis as a powerful tool for the transient dynamics of collective motions in lipid membranes on timescales that cannot be observed by any other technique.

TABLE 1 Concentrations used

Sample	χ_{DPPC}	χ_{DOPC}	χ_{Chol}	Two phases?
L_d-1	0.290	0.600	0.110	yes
L_d-2	0.269	0.636	0.094	yes
L_d-3	0.249	0.673	0.079	yes
Calculated L_d endpoint	0.24	0.69	0.07	–
L_d-4	0.228	0.709	0.063	no
L_d-5	0.207	0.746	0.047	no
L_d-6	0.186	0.782	0.031	no
L_d-7	0.166	0.819	0.016	no
L_d-8	0.145	0.855	0	no
L_o-1	0.547	0.148	0.305	yes
L_o-2	0.568	0.111	0.321	yes
Calculated L_o endpoint	0.58	0.09	0.33	–
L_o-3	0.589	0.074	0.337	no
L_o-4	0.610	0.037	0.353	no
L_o-5	0.631	0	0.369	no

These concentrations are shown graphically in Fig. 2. The calculated endpoints are the averages of the two concentrations on either side of the two-phase crossover (see Figs. S1 and S2).

MATERIALS AND METHODS

SAXS methods

Preparation of MLV samples for SAXS measurements

Multilamellar vesicle (MLV) samples of a desired composition and total mass of 2 mg were prepared from chloroform phospholipid and Chol stock solutions dispensed into a glass vial using a glass Hamilton syringe. Bulk chloroform was removed with a gentle dry nitrogen stream while heating the vials in a water bath set to 45°C, followed by high vacuum pumping overnight at room temperature. The dry films were hydrated with 0.100 mL of ultrapure water that was preheated to 45°C to produce MLVs. The MLV samples were held in a water bath at 45°C for ∼1 h with intermittent vigorous vortexing, followed by five freeze/thaw cycles between the water bath and a −80°C freezer. Samples were held in the dark at room temperature until measurement.

SAXS measurements

SAXS measurements were performed using a Rigaku BioSAXS-2000 home source system with a Pilatus 100K 2D detector and an HF007 copper rotating anode (Rigaku Americas, The Woodlands, TX, USA). MLV samples were loaded from 0.2 mL PCR strips into a fixed quartz capillary using a BioSAXS Automatic Sample Changer. The capillary temperature was held at 25°C with an external water chiller/heater. SAXS data were collected at a fixed sample-to-detector distance using a silver behenate calibration standard, with a total data collection time of 30 min. The 1D scattering intensity $I(q)$ ($q = 4\pi \sin(\theta)/\lambda$, where λ is the x-ray wavelength and 2θ is the scattering angle relative to the incident beam) was obtained by radial averaging of the corrected 2D image data, an operation that was performed automatically using Rigaku SAXSLab software. Data were collected in 5-min frames, with each frame processed separately to assess radiation damage; there were no significant changes in the scattering curves over time. Background scattering from water collected at the same temperature was subtracted from each frame, and the background-corrected $I(q)$ from the individual frames was then averaged, with the standard deviation taken to be the measurement uncertainty.

IXS methods

The IXS experiment was performed at the RIKEN Quantum NanoDynamics Beamline, BL43LXU (38), of the RIKEN SPring-8 Center. This beamline was chosen because it has the best available energy resolution and high intensity. In the present experiment, six analyzers were used, having approximately Lorentzian resolution with a full width at half maximum between 0.79 and 0.95 meV at 25.7 keV ($\Delta E/E < 5\times10^{-8}$) depending on the analyzer (39,40). These resolution functions were measured using a standard PMMA scatterer at the maximum of its structure factor as detailed in (39,40). An IXS experiment measures the scattered intensity, which is directly proportional to the dynamic structure factor $S(Q, \omega)$, where $\hbar\omega$ is the energy transfer and Q is the momentum transfer (for an example for a spectrum, see Fig. 1 *b*). In the present case, the geometry is chosen so that Q is in the plane of the membrane, so we probe only in-plane atomic motion. Over the frequency range accessed by these measurements, the dynamics of the system at each Q were well described by a few damped harmonic oscillator (DHO) modes (21,30), which is the simplest, lowest-order approximation to a finite width phonon line. In addition, there is a strong elastic component in the present spectra resulting from the lack of long-range order. Each spectrum at a particular momentum transfer, Q, is therefore fit to the sum of an elastic line (δ function) and several DHO lines of the form

$$L_i(\omega) = \frac{A_i\Gamma_i\Omega_i^2}{\left(\omega^2 - \Omega_i^2\right)^2 + \Gamma_i^2\omega^2}. \quad (1)$$

For comparison with the measurements, the sum is scaled by a detailed balance factor and convolved with the resolution. The mode frequencies Ω_i, amplitudes A_i, and widths Γ_i at each Q are determined by least-squares fitting. The optimal number of DHO modes used to fit the IXS data as shown in Figs. S12 and S13 was determined through a procedure based on residual and χ^2 statistical analysis, described in detail in our previous work in (21). The dispersion relations for the phonon modes can be observed by plotting the Ω_i as a function of Q, as shown in Fig. 3.

Sample preparation

All lipids (DPPC/DOPC/Chol) were purchased from Sigma-Aldrich and used without further purification. Stock solutions with lipid concentrations of 20 mg/mL were prepared in 2,2,2-trifluoroethanol solvent. The ternary lipid mixtures for the L_o and L_d phases were prepared using the molar ratios (χ_{DPPC}:χ_{DOPC}:χ_{Chol}) of the calculated L_o (0.24:0.69:0.07) and L_d (0.58:0.09:0.33) endpoints, respectively, determined from the SAXS tie-line results in Table 1. To facilitate the IXS measurements, a synthetic diamond single crystal (4.5 × 4.5 mm^2, 0.5 mm thick, (100) face orientation) was used as a substrate. The crystal was cleaned with consecutive rinses of chloroform, methanol, and deionized water and then UV/ozone etched for 30 min before lipid solution deposition. Solutions were spin coated on the diamond substrate and spun for 60 s at 300 rpm to prepare oriented lipid stacks, with a total thickness of ∼50 μm, or about 8300 bilayers, thick enough to limit interaction of the x-ray beam with the diamond substrate. The samples were dried in a vacuum oven at room temperature for 24 h to remove any remaining traces of solvent prior to the IXS measurements.

IXS measurement

The IXS spectra for both the L_o and L_d samples, presented in Figs. S12 and S13, respectively, were measured at 25°C and ambient pressure in a custom-made humidity and temperature control chamber at a relative humidity of > 98%. The saturated water vapor for the humidity was generated using an ultrasonic transducer from a water bath directly connected to the chamber and circulated using a small internal fan to ensure uniform humidity distribution inside the chamber. The relative humidity was monitored continuously using a factory-calibrated Rotronics humidity probe HC2-C05 placed in the immediate vicinity of the sample and maintained at the setpoint in a closed loop using a custom-built controller (GEOCalibration) during the IXS measurements. The temperature of the chamber and the sample was controlled and maintained at 25°C using a recirculating water chiller.

The IXS spectra for each sample were measured at 12 discrete momentum transfers over the range of 1.5–17.96 nm^{-1}. The incident beam with 5×10^9 photons/s was focused to a spot size of 50×50 μm^2 on the sample. To avoid beam damage, the sample was repositioned every 2 h to a fresh spot for new scans. At the end of the measurement, the resulting scans at the same Q were compared to ensure no noticeable differences before they were summed and analyzed. Potential beam damage was also assessed by measuring the $S(q)$ of the sample every 2 h, which showed no noticeable changes. The spectra, together with the DHO fitted spectra and the normalized residuals, are presented in Figs. S12 and S13.

Simulation methods

Simulation setup and parameters

The simulated systems were built using the CHARMM-GUI, and minimization and initial equilibration were performed using the default protocol obtained from the CHARMM-GUI (41–46). The compositions of the systems studied here were obtained from updated the $L_o - L_d$ tie-line compositions measured via SAXS (see Fig. 1 *c*). They were initialized in a roughly $10\times$ 10 nm^2 box, with 4 nm of TIP3P water (47) above and below the bilayer, resulting in a roughly $(10\ nm)^3$ cube. The lipids were modeled with the CHARMM36 force field (48). Both simulations used a standard VFSWITCH truncation over the interval of 8–12 Å. The simulations were run in GROMACS 2019.2 using the "md" leapfrog integrator after an initial minimization step using the steepest descent integrator "steep." The first three of the seven equilibration steps used a 1 fs integration step, while the remainder and the production runs used a 2 fs time step. Electrostatics were calculated using PME (49,50). In the production simulations, temperature control used the Nose-Hoover extended ensemble method (51,52), with a temperature coupling constant of 1 ps for the lipids and water separately. Pressure control used the Parrinello-Rahman extended ensemble method (53), with a pressure of 1 bar coupled semi-isotropically, a compressibility of 4.5×10^{-5} bar^{-1}, and a pressure coupling constant of 5 ps (for further details on the CHARMM-GUI equilibration steps, see Table S1). This was followed by a longer equilibration step totaling 500 ns to ensure the lipids and Chol were fully mixed and the box size fully relaxed, using the Parrinello-Rahman barostat and the Nosé-Hoover thermostat. This was followed by an 11 ns production simulation under constant volume also using the Nosé-Hoover thermostat. Throughout, hydrogen bonds were constrained using the default LINCS protocol.

Simulation analysis

In simulations, the time-dependent correlations of the particle currents $C(Q,\omega)$ are calculated, which are related to the dynamic structure factor by $C(Q,\omega) = S(Q,\omega)\cdot\omega^2/Q^2$. The (spatial Fourier transformed) particle currents are defined by

$$\mathbf{J}(\mathbf{Q}_i,t) = \sum_{\alpha \in \text{ atoms}} \mathbf{v}_\alpha(t) e^{-i\mathbf{r}_\alpha(t)\cdot\mathbf{Q}_i}, \tag{2}$$

where $\mathbf{v}_\alpha(t)$ is the velocity of atom α at time t and $\mathbf{r}_\alpha(t)$ is its position. The scattering vectors were sampled randomly within the Q range of interest, $\|\mathbf{Q}\| \in$ 1.5–16.5 nm^{-1}, and only with allowable wavevectors, i.e., those of the form

$$\langle Q_x, Q_y, Q_z\rangle = \left\langle n_x\frac{2\pi}{L_x}, n_y\frac{2\pi}{L_y}, 0\right\rangle, \tag{3}$$

for integer $n_{x,y}$, where L_x and L_y are the simulation dimensions in the membrane plane. Because the experiment measures only the longitudinal component of the correlation function, here, $C(Q,\omega)$ is reported only for the parallel current:

$$C_\parallel(Q,t) = \langle J_\parallel(Q,t) J_\parallel(Q,0)\rangle, \tag{4}$$

with the parallel component of $\mathbf{J}$ obtained by

$$J_\parallel(Q_i) = \hat{\mathbf{Q}}_i \cdot \mathbf{J}(\mathbf{Q}_i) \tag{5}$$

and then orientationally averaged and binned to the nearest integer nm^{-1} (i.e., bins of $Q \in \{1.5\text{–}2.5\ nm^{-1}\}$ … $\{15.5\text{–}16.5\ nm^{-1}\}$).

Following the same treatment as the experimental data, for each Q, the dynamic structure factor $S(Q,\omega)$ was obtained from the longitudinal current correlation spectrum and fit to three or four DHO modes. For some wavenumbers, it was not clear whether the data were best fit by three or four DHO modes; in these cases, a test using the Bayesian information criterion indicated that three DHO modes was the better choice (details are provided in the supporting material). All of the fits are shown in Figs. S6–S11. From this analysis, phonon dispersions $\omega(Q)$ are obtained, shown on the right side of Fig. 3. For each system, the speed of sound was obtained by fitting the acoustic mode (*green line* in Fig. 3) below $Q = 8\ nm^{-1}$ to a sine function and extrapolating to $Q = 0$.

RESULTS

Compositions of L_o and L_d phases

For this work, it is essential that the system be in a single phase (either L_o or L_d) in order to simplify the interpretation of the phonon spectra. The lipid mixtures reported here were therefore prepared at the endpoints of a tie line inside the L_o-L_d coexistence region of the ternary phase diagram. The orientation of this tie line and the location of its endpoints (i.e., the compositions of the L_o and L_d phases) were previously determined by ^{2}H-NMR (35). However, SAXS measurements suggested that these endpoints are slightly inside the coexistence region. Revised endpoints are presented in Fig. 1, and the L_o and L_d compositions are reported in Table 1.

Two samples were first prepared at compositions corresponding to the reported L_o and L_d endpoints (54). The L_o endpoint produced five Bragg reflections corresponding to a lamellar repeat distance of 6.88 nm, consistent with substantial hydrocarbon chain order due to the high concentration of DPPC and Chol (Fig. S1). In contrast, the L_d endpoint sample produced only two clear Bragg reflections with a lamellar repeat distance of 6.50 nm and a substantial amount of diffuse scattering, suggesting a disordered bilayer (Fig. S1). Interestingly, each sample produced a second, less intense set of Bragg reflections that was most apparent in the second-order peak near 2 nm^{-1}. In the L_d endpoint sample, the minor peak corresponded to the larger repeat distance of 7.02 nm, similar to the dominant peak in the L_o sample. Conversely, in the L_o endpoint sample, the minor peak corresponded to a smaller repeat distance of 6.43 nm, similar to the dominant peak in the L_d sample. These observations are consistent with each sample being located near the end of a tie line but still within the phase coexistence region at 25°C.

To locate the tie-line endpoints more precisely, we prepared and measured a series of samples whose compositions

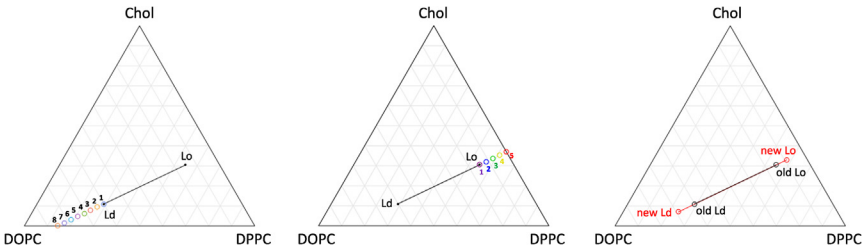

FIGURE 2 Tie-line concentrations tested for L_d (*left*) and L_o (*center*) and final determination of tie-line endpoints as compared to previously determined endpoints (*right*).

extended the original NMR-determined tie line in both directions (i.e., from the NMR-determined L_d endpoint toward the binary DOPC/DPPC axis and from the NMR-determined L_o endpoint toward the binary DPPC/Chol axis), as shown in Fig. 2. The compositions of these samples are given in Table 1. In the L_d set, the first- and second-order Bragg reflections corresponding to a thicker L_o phase were clearly visible in samples 2 and 3 but were undetectable in sample 4. Similarly, in the L_o set, a second-order reflection corresponding to the thinner L_d phase is clearly present in sample 2 but not sample 3. In both cases, a revised phase boundary was estimated to be the midpoint between the last sample showing two components and the first sample showing only a single component. These compositions are 0.24 : 0.69 : 0.07 for L_o and 0.58 : 0.09 : 0.33 for L_d.

Phonon dispersions in L_o and L_d

As described in the materials and methods, for each Q, the dynamic structure factor $S(Q,\omega)$ is fit to a sum of DHO modes. By plotting the frequencies of these modes over the entire Q range, the phonon dispersions are obtained, as shown in Fig. 3. For $Q < 5$ nm^{-1}, the data are fit well by a sum of two DHO modes, indicating that there are two phonon branches for this Q range (see *all four boxes* in Fig. 3). For larger Q values, the L_o systems require three DHO modes; the simulated L_d system also required a third mode, but this mode was at a significantly lower intensity than the others and may not be resolvable in the experiment. (The fits to the simulation data also included a higher-energy branch not shown on the scale in Fig. 3.).

The acoustic modes (*green series* in Fig. 3) indicate the edge of the first Brillouin zone at about 15 nm^{-1} (identified as the minimum in the main acoustic mode and corresponding to the distance between hydrocarbon chains). The speeds of sound are similar, equal to the slope of the acoustic mode as $Q \to 0$, roughly 2.6 and 2.4 km s^{-1} for the experimental L_o and L_d systems, respectively, while for the simulated systems, they were 3.0 and 2.8 km s^{-1}, respectively. (These were obtained by fitting the acoustic mode over $Q \leq 8$ nm^{-1} to a sinusoid and extrapolating to $Q = 0$.) The faster speed of sound in the L_o phase is expected based on the higher molecular density of this phase.

All four systems also present a low-energy phonon mode (*orange series* in Fig. 3). Intriguingly, this mode is present in many different soft- and biomaterials and is located at approximately 1 meV (55). This energy range of around 1 meV is a common location for the transverse acoustic phonons in noncrystalline materials. However, its nondispersive behavior, as shown in Fig. 3, indicates a possible coexistence of acoustic and optical phonon modes, as previously observed in lipid-like mesogenic systems (56).

Also clearly observed in the L_o systems is an intermediate-energy, truncated optical mode (*purple series* in Fig. 3) at around 5 meV with an energy gap at low Q. A similarly gapped optical mode was also observed recently in L_o phase binary mixtures (30) of DPPC and Chol. In the simulated L_o system, this mode shows some dispersion—having a slightly higher energy than observed in the experiment, the high-Q part of the dispersion is pushed to lower energy. In the L_d simulation, a lower-intensity remnant of this mode is observed (at most 4% of the total signal intensity, compared to 8% in L_o, and over a limited Q range), apparently too low in intensity to be observed experimentally (see the lack of a 3 meV optical mode in Figs. 3 and S13 for the experimental spectra with DHO fits). As discussed below, this gapped optical mode reports on structures within the L_o phase.

DISCUSSION

The low-Q gap in the optical mode is consistent with a finite-size confinement effect: similar analysis of the phonon density of states for simulated nanocrystals reveals a lack of phonons at low Q values, confined by the size of the nanocrystal (57). In the present case, a low-Q phonon gap at roughly 5 nm^{-1} would correspond to a confinement distance of 1.3 nm, almost exactly 3 times the in-plane hydrocarbon chain distance, as revealed by the chain-chain radial distribution function measured in the simulations (Fig. S14). Thus, the low-Q gap suggests a crystalline-like cluster about three hydrocarbon chains across. This is consistent with a nanoscale substructure of hexagonally packed hydrocarbon chains, previously reported by Lyman and co-workers (36,37), subsequently verified by NMR (58), and apparent upon visual inspection in Fig. 4. The precise location of the peaks in the radial distribution function may change slightly with different force fields, but we expect that the gapped mode will be observed in any multicomponent system that displays the hexagonal substructure. The effect of

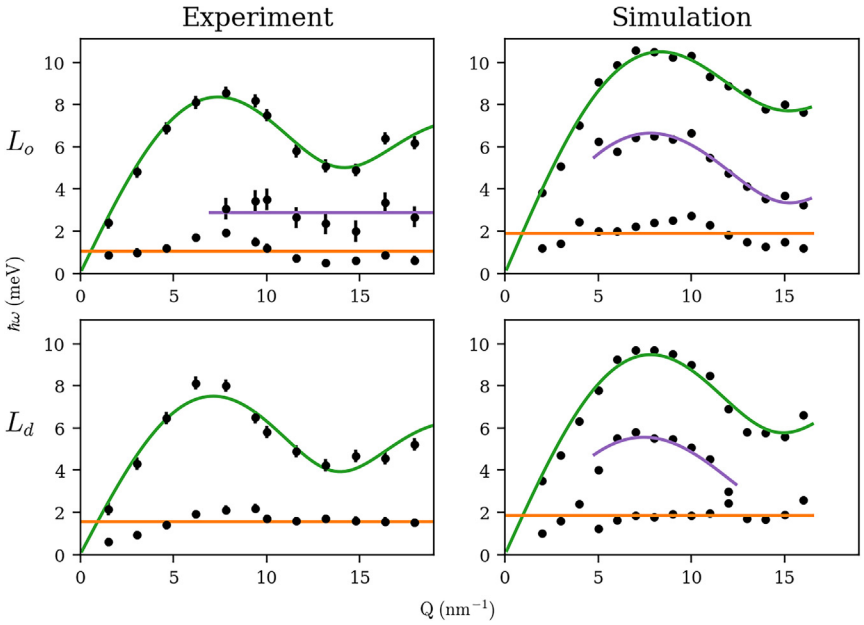

FIGURE 3 Fitting results for the data from both IXS experiment (*left*) and MD simulation (*right*) for the L_o system (*top*) and L_d system (*bottom*). Curves are to guide the eye. Error bars represent the range of DHO model parameters that are consistent with a 95% confidence interval.

local ordering and its coupling to dynamics has also been studied recently by Srivastava and co-workers, who imported ideas on nonaffine displacements from the literature on glassy systems. These ideas may yield additional insight into the origin of gapped modes in membranes (59–61).

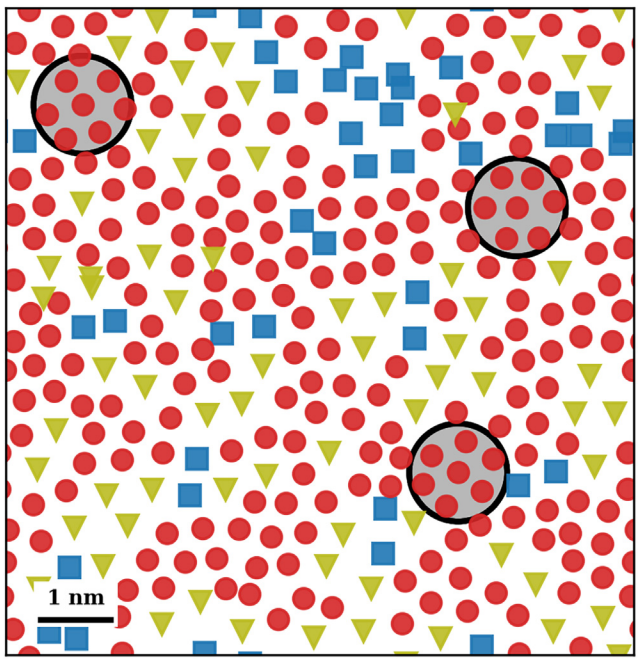

FIGURE 4 A snapshot of one frame of the L_o simulation, showing the in-plane projections of the centers of mass of cholesterol and of the tails of each lipid. Small red circles are DPPC tails, blue squares are DOPC tails, and each yellow triangle shows the center of mass of one cholesterol molecule. The large black circles mark examples of the largest clusters of DPPC lipids within which no optical modes would be supported.

State-of-the-art IXS measurements like those presented here offer a unique window into the fast, collective dynamics of lipid membranes. Most prior work has been focused on single-component membranes (21,25,29,31,32), showing that molecular simulations quantitatively reproduce the dynamics observed by IXS and offering insights into how the fast, elastic response crosses over into the viscous regime. More recent work identified a new optical mode with a low-Q gap in a binary mixture of DPPC and Chol, at a temperature and composition that are in the L_o phase. The same binary mixture was also shown in earlier simulations (62) to present the transient hexagonal packing of hydrocarbon chains that is a signature of the L_o phase and first reported in ternary mixtures of DPPC/DOPC/Chol (36). The emergence of the truncated optical mode might presage a qualitative change in the longer-wavelength dynamics of membranes, as Chol sufficient to induce the L_o phase increases the membrane's viscosity by up to an order of magnitude (12).

The results presented here show that this nanoscale structure reveals itself in the phonon modes observed by IXS. Detection of the 5 meV gapped optical mode might therefore serve as a useful indicator of the extent to which the dynamics and structure of more complex lipid mixtures (for example, mimicking the outer leaflet of the plasma membrane (63)) are captured by simpler model membranes.

ACKNOWLEDGMENTS

The work at the National Synchrotron Light Source-II (NSLS-II), Brookhaven National Laboratory, was supported by the US Department of Energy, Office of Science, Office of Basic Energy Sciences, under contract DE-SC0012704. D.B. is supported through the National Science

Foundation, Division of Molecular and Cellular Biosciences (MCB), under contract no. 2219289. We thank Yuki Takayama for assistance in sample preparation for the experiments at SPring-8 and Swapnil Baral for preliminary simulations. E.R.L. and J.E.F. were supported by NSF MCB 2121854 and Brookhaven National Lab award 383344. This work used Bridges-2 at Pittsburgh Supercomputing Center through allocation BIO230093 from the Advanced Cyberinfrastructure Coordination Ecosystem: Services & Support (ACCESS) program, which is supported by National Science Foundation grants 2138259, 2138286, 2138307, 2137603, and 2138296.

AUTHOR CONTRIBUTIONS

E.R.L. and J.E.F. designed and carried out the simulations, J.E.F. and D.B. developed the simulation analysis, F.A.H. performed the SAXS experiments and data analysis, Y.Q.C. and M.Z. designed the IXS experiments. D.S., Y.Q.C., D.I., A.Q.R.B., and M.Z. carried out the IXS experiments and data analysis. J.E.F., E.R.L., and D.B. drafted and edited the manuscript.

DECLARATION OF INTERESTS

The authors declare no competing interests.

SUPPORTING CITATIONS

Reference (64) appears in the supporting material.

SUPPORTING MATERIAL

Supporting material can be found online at https://doi.org/10.1016/j.bpj.2024.10.017.

REFERENCES

1. Singer, S. J., and G. L. Nicolson. 1972. The Fluid Mosaic Model of the Structure of Cell Membranes. *Science.* 175:720–731. https://doi.org/10.1126/science.175.4023.720.
2. Sinensky, M. 1974. Homeoviscous Adaptation–A Homeostatic Process that Regulates the Viscosity of Membrane Lipids in Escherichia coli. *Proc. Natl. Acad. Sci. USA.* 71:522–525. issn: 0027-8424. https://doi.org/10.1073/pnas.71.2.522.
3. Saffman, P. G., and M. Delbrück. 1975. Brownian motion in biological membranes. *Proc. Natl. Acad. Sci. USA.* 72:3111–3113. issn: 00278424. https://doi.org/10.1073/PNAS.72.8.3111.
4. Budin, I., T. de Rond, …, J. D. Keasling. 2018. Viscous control of cellular respiration by membrane lipid composition. *Science.* 362:1186–1189. issn: 0036-8075. https://doi.org/10.1126/science.aat7925.
5. Ballweg, S., E. Sezgin, …, R. Ernst. 2020. Regulation of lipid saturation without sensing membrane fluidity. *Nat. Commun.* 11:756–1723. https://doi.org/10.1038/s41467-020-14528-1.
6. Chwastek, G., E. P. Petrov, and J. P. Sáenz. 2020. A Method for High-Throughput Measurements of Viscosity in Sub-micrometer-Sized Membrane Systems. *Chembiochem.* 21:836–844. issn: 14397633. https://doi.org/10.1002/CBIC.201900510.
7. Pandey, B. N., and K. P. Mishra. 1999. Radiation induced oxidative damage modification by cholesterol in liposomal membrane. *Radiat. Phys. Chem.* 54:481–489. issn: 0969806X. https://doi.org/10.1016/S0969-806X(98)00297-7.
8. Cicuta, P., S. L. Keller, and S. L. Veatch. 2007. Diffusion of Liquid Domains in Lipid Bilayer Membranes. *J. Phys. Chem. B.* 111:3328–3331. issn: 1520-6106. https://doi.org/10.1021/jp0702088.
9. Hormel, T. T., S. Q. Kurihara, …, R. Parthasarathy. 2014. Measuring lipid membrane viscosity using rotational and translational probe diffusion. *Phys. Rev. Lett.* 112:188101–188105. issn: 10797114. https://doi.org/10.1103/PhysRevLett.112.188101.
10. Camley, B. A., C. Esposito, …, F. L. H. Brown. 2010. Lipid Bilayer Domain Fluctuations as a Probe of Membrane Viscosity. *Biophys. J.* 99:L44–L46. https://doi.org/10.1016/j.bpj.2010.07.007.
11. Honerkamp-Smith, A. R., F. G. Woodhouse, …, R. E. Goldstein. 2013. Membrane viscosity determined from shear-driven flow in giant vesicles. *Phys. Rev. Lett.* 111:038103. issn: 00319007. https://doi.org/10.1103/PHYSREVLETT.111.038103.
12. Faizi, H. A., R. Dimova, and P. M. Vlahovska. 2022. A vesicle microrheometer for high-throughput viscosity measurements of lipid and polymer membranes. *Biophys. J.* 121:910–918. issn: 00063495. https://doi.org/10.1016/j.bpj.2022.02.015.
13. Nagao, M., E. G. Kelley, …, P. D. Butler. 2021. Relationship between Viscosity and Acyl Tail Dynamics in Lipid Bilayers. *Phys. Rev. Lett.* 127:078102. issn: 1079-7114. https://doi.org/10.1103/PhysRevLett.127.078102.
14. Fitzgerald, J. E., R. M. Venable, …, E. R. Lyman. 2023. Surface viscosities of lipid bilayers determined from equilibrium molecular dynamics simulations. *Biophys. J.* issn: 00063495. https://doi.org/10.1016/J.BPJ.2023.01.038.
15. Zgorski, A., R. W. Pastor, and E. Lyman. 2019. Surface Shear Viscosity and Interleaflet Friction from Nonequilibrium Simulations of Lipid Bilayers. *J. Chem. Theor. Comput.* 15:6471–6481. issn: 15499626. https://doi.org/10.1021/acs.jctc.9b00683.
16. Nagao, M., E. G. Kelley, …, P. D. Butler. 2017. Probing Elastic and Viscous Properties of Phospholipid Bilayers Using Neutron Spin Echo Spectroscopy. *J. Phys. Chem. Lett.* 8:4679–4684. issn: 1948-7185. https://doi.org/10.1021/acs.jpclett.7b01830.
17. Kelley, E. G., P. D. Butler, and M. Nagao. 2021. Collective dynamics in lipid membranes containing transmembrane peptides. *Soft Matter.* 17:5671–5681. issn: 1744-683X. https://doi.org/10.1039/D1SM00314C.
18. Rheinstädter, M. C., W. Häussler, and T. Salditt. 2006. Dispersion Relation of Lipid Membrane Shape Fluctuations by Neutron Spin-Echo Spectrometry. *Phys. Rev. Lett.* 97:048103. issn: 0031-9007. https://doi.org/10.1103/PhysRevLett.97.048103.
19. Chakraborty, S., M. Doktorova, …, R. Ashkar. 2020. How cholesterol stiffens unsaturated lipid membranes. *Proc. Natl. Acad. Sci. USA.* 117:21896–21905. issn: 10916490. https://doi.org/10.1073/pnas.2004807117.
20. Pan, J., X. Cheng, …, J. Katsaras. 2015. Structural and mechanical properties of cardiolipin lipid bilayers determined using neutron spin echo, small angle neutron and X-ray scattering, and molecular dynamics simulations. *Soft Matter.* 11:130–138. issn: 1744-683X. https://doi.org/10.1039/C4SM02227K.
21. Zhernenkov, M., D. Bolmatov, …, Y. Q. Cai. 2016. Revealing the mechanism of passive transport in lipid bilayers via phonon-mediated nanometre-scale density fluctuations. *Nat. Commun.* 7:11575.
22. D'Angelo, G., V. C. Nibali, …, A. Paciaroni. 2018. Multiple interacting collective modes and phonon gap in phospholipid membranes. *J. Phys. Chem. Lett.* 9:4367–4372.
23. Baron, A. Q. 2016. High-Resolution Inelastic X-Ray Scattering I: Context, Spectrometers, Samples, and Superconductors. Springer International Publishing, pp. 1643–1719. https://doi.org/10.1007/978-3-319-14394-1_41.
24. Sette, F., G. Ruocco, …, R. Verbeni. 1995. Collective Dynamics in Water by High Energy Resolution Inelastic X-Ray Scattering. *Phys. Rev. Lett.* 75:850–853.
25. Bolmatov, D., M. Zhernenkov, …, A. Cunsolo. 2015. Revealing the mechanism of the viscous-to-elastic crossover in liquids. *J. Phys. Chem. Lett.* 6:3048–3053.
26. Bolmatov, D., M. Zhernenkov, …, Y. Q. Cai. 2016. Thermally triggered phononic gaps in liquids at THz scale. *Sci. Rep.* 6:19469.
27. Ishikawa, D., and A. Q. Baron. 2021. Interaction of Acoustic and Quasi-Elastic Modes in Liquid Water on Nanometer Length Scales

Journal of the Physical Society of Japan. *J. Physical Soc. Japan.* 90:083602. issn: 0031-9015. https://doi.org/10.7566/JPSJ.90.083602.

28. Bolmatov, D., Q. Zhang, …, J. Katsaras. 2018. Nanoscale Q-resolved phonon dynamics in block copolymers. *ACS Appl. Nano Mater.* 1:4918–4926.
29. Bolmatov, D., M. Zhernenkov, …, A. Cunsolo. 2017. Emergent optical phononic modes upon nanoscale mesogenic phase transitions. *Nano Lett.* 17:3870–3876.
30. Soloviov, D., Y. Q. Cai, …, M. Zhernenkov. 2020. Functional lipid pairs as building blocks of phase-separated membranes. *Proc. Natl. Acad. Sci. USA.* 117:4749–4757. issn: 0027-8424. https://doi.org/10.1073/pnas.1919264117.
31. Bolmatov, D., D. Soloviov, …, J. Katsaras. 2020. Molecular picture of the transient nature of lipid rafts. *Langmuir.* 36:4887–4896.
32. Bolmatov, D., Y. Q. Cai, …, M. Zhernenkov. 2018. Crossover from picosecond collective to single particle dynamics defines the mechanism of lateral lipid diffusion. *Biochim. Biophys. Acta Biomembr.* 1860:2446–2455.
33. Bolmatov, D., C. P. Collier, …, J. Katsaras. 2023. Real Space and Time Imaging of Collective Headgroup Dipole Motions in Zwitterionic Lipid Bilayers. *Membranes.* 13:442.
34. Bolmatov, D., J. J. Kinnun, …, M. O. Lavrentovich. 2020. Phonon-mediated lipid raft formation in biological membranes. *Chem. Phys. Lipids.* 232:104979.
35. Veatch, S. L., I. V. Polozov, …, S. L. Keller. 2004. Liquid Domains in Vesicles Investigated by NMR and Fluorescence Microscopy. *Biophys. J.* 86:2910–2922. issn: 00063495. https://doi.org/10.1016/S0006-3495(04)74342-8.
36. Sodt, A. J., M. L. Sandar, …, E. Lyman. 2014. The Molecular Structure of the Liquid-Ordered Phase of Lipid Bilayers. *J. Am. Chem. Soc.* 136:725–732. issn: 0002-7863. https://doi.org/10.1021/ja4105667.
37. Sodt, A. J., R. W. Pastor, and E. Lyman. 2015. Hexagonal Substructure and Hydrogen Bonding in Liquid-Ordered Phases Containing Palmitoyl Sphingomyelin. *Biophys. J.* 109:948–955. issn: 00063495. https://doi.org/10.1016/j.bpj.2015.07.036.
38. Baron, A. Q. R. 2010. Status of the RIKEN Quantum NanoDynamics Beamline (BL43LXU): The Next Generation for Inelastic X-Ray Scattering. https://user.spring8.or.jp/sp8info/?p=3138.
39. Ishikawa, D., D. S. Ellis, …, A. Q. R. Baron. 2015. Inelastic X-ray scattering with 0.75 meV resolution at 25.7 keV using a temperature-gradient analyzer. *J. Synchrotron Radiat.* 22:3–9. issn: 1600-5775. https://doi.org/10.1107/S1600577514021006.
40. Ishikawa, D., and A. Q. R. Baron. 2021. Practical measurement of the energy resolution for meV-resolved inelastic X-ray scattering. *J. Synchrotron Radiat.* 28:804–811. https://doi.org/10.1107/S1600577521003234.
41. Jo, S., T. Kim, …, W. Im. 2008. CHARMM-GUI: A web-based graphical user interface for CHARMM. *J. Comput. Chem.* 29:1859–1865. issn: 1096-987X. https://doi.org/10.1002/JCC.20945.
42. Jo, S., T. Kim, and W. Im. 2007. Automated Builder and Database of Protein/Membrane Complexes for Molecular Dynamics Simulations. *PLoS One.* 2:e880–e6203. https://doi.org/10.1371/JOURNAL.PONE.0000880.
43. Wu, E. L., X. Cheng, …, W. Im. 2014. CHARMM-GUI Membrane Builder toward realistic biological membrane simulations. *J. Comput. Chem.* 35:1997–2004. issn: 1096-987X. https://doi.org/10.1002/JCC.23702.
44. Lee, J., X. Cheng, …, W. Im. 2016. CHARMM-GUI Input Generator for NAMD, GROMACS, AMBER, OpenMM, and CHARMM/OpenMM Simulations Using the CHARMM36 Additive Force Field. *J. Chem. Theor. Comput.* 12:405–413. issn: 15499626. https://doi.org/10.1021/ACS.JCTC.5B00935.
45. Brooks, B. R., C. L. Brooks, …, M. Karplus. 2009. CHARMM: The biomolecular simulation program. *J. Comput. Chem.* 30:1545–1614. issn: 1096-987X. https://doi.org/10.1002/JCC.21287.
46. Jo, S., T. Kim, …, W. Im. 2008. CHARMM-GUI: A web-based graphical user interface for CHARMM. *J. Comput. Chem.* 29:1859–1865. issn: 1096-987X. https://doi.org/10.1002/JCC.20945.
47. Jorgensen, W. L., J. Chandrasekhar, …, M. L. Klein. 1983. Comparison of simple potential functions for simulating liquid water. *J. Chem. Phys.* 79:926–935. issn: 0021-9606. https://doi.org/10.1063/1.445869.
48. Klauda, J. B., R. M. Venable, …, R. W. Pastor. 2010. Update of the CHARMM all-atom additive force field for lipids: validation on six lipid types. *J. Phys. Chem. B.* 114:7830–7843. issn: 1520-7843. https://doi.org/10.1021/jp101759q.
49. Darden, T., D. York, and L. Pedersen. 1993. Particle mesh Ewald: An N ·log(N) method for Ewald sums in large systems. *J. Chem. Phys.* 98:10089–10092. issn: 0021-9606. https://doi.org/10.1063/1.464397.
50. Essmann, U., L. Perera, …, L. G. Pedersen. 1995. A smooth particle mesh Ewald method. *J. Chem. Phys.* 103:8577–8593. issn: 0021-9606. https://doi.org/10.1063/1.470117.
51. Nosé, S. 1984. A molecular dynamics method for simulations in the canonical ensemble. *Mol. Phys.* 52:255–268. issn: 0026-8976. https://doi.org/10.1080/00268978400101201.
52. Hoover, W. G. 1985. Canonical dynamics: Equilibrium phase-space distributions. *Phys. Rev.* 31:1695–1697. issn: 0556-2791. https://doi.org/10.1103/PhysRevA.31.1695.
53. Parrinello, M., and A. Rahman. 1981. Polymorphic transitions in single crystals: A new molecular dynamics method. *J. Appl. Phys.* 52:7182–7190. issn: 0021-8979. https://doi.org/10.1063/1.328693.
54. Veatch, S. L., O. Soubias, …, K. Gawrisch. 2007. Critical fluctuations in domain-forming lipid mixtures. *Proc. Natl. Acad. Sci. USA.* 104:17650–17655. issn: 0027-8424. https://doi.org/10.1073/pnas.0703513104.
55. Bolmatov, D. 2022. The phonon theory of liquids and biological fluids: Developments and applications. *J. Phys. Chem. Lett.* 13:7121–7129.
56. Bolmatov, D., D. Soloviov, …, J. Katsaras. 2018. Anomalous nanoscale optoacoustic phonon mixing in nematic mesogens. *J. Phys. Chem. Lett.* 9:2546–2553.
57. Şopu, D., J. Kotakoski, and K. Albe. 2011. Finite-size effects in the phonon density of states of nanostructured germanium: A comparative study of nanoparticles, nanocrystals, nanoglasses, and bulk phases. *Phys. Rev. B.* 83:245416. issn: 1098-0121. https://doi.org/10.1103/PhysRevB.83.245416.
58. Yano, Y., S. Hanashima, …, M. Murata. 2020. Sphingomyelins and ent-Sphingomyelins Form Homophilic Nano-Subdomains within Liquid Ordered Domains. *Biophys. J.* 119:539–552. issn: 00063495. https://doi.org/10.1016/j.bpj.2020.06.028.
59. Iyer, S. S., M. Tripathy, and A. Srivastava. 2018. Fluid Phase Coexistence in Biological Membrane: Insights from Local Nonaffine Deformation of Lipids. *Biophys. J.* 115:117–128. issn: 00063495. https://doi.org/10.1016/j.bpj.2018.05.021.
60. Tripathy, M., and A. Srivastava. 2023. Lipid packing in biological membranes governs protein localization and membrane permeability. *Biophys. J.* 122:2727–2743. issn: 00063495. https://doi.org/10.1016/j.bpj.2023.05.028.
61. Tripathy, M., and A. Srivastava. 2024. Non-affine deformation analysis and 3D packing defects: A new way to probe membrane heterogeneity in molecular simulations. *Methods Enzymol.* 701:541–577. https://doi.org/10.1016/bs.mie.2024.03.011.
62. Javanainen, M., H. Martinez-Seara, and I. Vattulainen. 2017. Nanoscale Membrane Domain Formation Driven by Cholesterol. *Sci. Rep.* 7:1143. issn: 2045-2322. https://doi.org/10.1038/s41598-017-01247-9.
63. Lorent, J. H., K. R. Levental, …, I. Levental. 2020. Plasma membranes are asymmetric in lipid unsaturation, packing and protein shape. *Nat. Chem. Biol.* 16:644–652. issn: 1552-4450. https://doi.org/10.1038/s41589-020-0529-6.
64. Savitzky, A., and M. J. E. Golay. 1964. Smoothing and Differentiation of Data by Simplified Least Squares Procedures. *Anal. Chem.* 36:1627–1639. issn: 0003-2700. https://doi.org/10.1021/ac60214a047.